Astronomy & Astrophysics manuscript no. GJ9827paper
February 28, 2018

Mass determination of the 1:3:5 near-resonant planets transiting GJ 9827 (K2-135) ⋆

J. Prieto-Arranz[1,2], E. Palle[1,2], D. Gandolfi[3], O. Barragán[3], E.W. Guenther[1,4], F. Dai[5,6], M. Fridlund[7,8], T. Hirano[9], J. Livingston[10], P. Niraula[11], C. M. Persson[8], S. Redfield[11], S. Albrecht[12], R. Alonso[1,2], G. Antoniciello[3], J. Cabrera[13], W. D. Cochran[14], Sz. Csizmadia[13], H. Deeg[1,2], Ph. Eigmüller[13], M. Endl[14], A. Erikson[13], M. E. Everett[15], A. Fukui[16], S. Grziwa[17], A. P. Hatzes[4], D. Hidalgo[1,2], M. Hjorth[12], J. Korth[17], D. Lorenzo-Oliveira[18], F. Murgas[1,2], N. Narita[10,19,20], D. Nespral[1,2], G. Nowak[1,2], M. Pätzold[17], P. Montañes Rodríguez[1,2], H. Rauer[13,21], I. Ribas[22,23], A. M. S. Smith[13], V. Van Eylen[7], and J. N. Winn[5]

(Affiliations can be found after the references)

Received dd mmm yyyy; accepted dd mmm yyyy

ABSTRACT

Context. Multi-planet systems are excellent laboratories to test planet formation models, since all planets are formed under the same initial conditions. In this context, systems transiting bright stars can play a key role, since planetary masses, radii, and bulk densities can be accurately measured.

Aims. GJ 9827 (K2-135) has recently been found to host a tightly packed system consisting of three transiting small planets whose orbital periods of 1.2, 3.6, and 6.2 days are near the 1:3:5 ratio. GJ 9827 hosts the nearest planetary system (d = 30.32 ± 1.62 pc) detected by *Kepler* and *K2*. Its brightness (V = 10.35 mag) makes the star an ideal target for detailed studies of the properties of its planets.

Methods. Combining the *K2* photometry with high-precision radial-velocity measurements gathered with the FIES, HARPS, and HARPS-N spectrographs we revise the system parameters and derive the masses of the three planets.

Results. We find that GJ 9827 b has a mass of $M_b = 3.74^{+0.50}_{-0.48}\,M_\oplus$ and a radius of $R_b = 1.62^{+0.17}_{-0.16}\,R_\oplus$, yielding a mean density of $\rho_b = 4.81^{+1.97}_{-1.33}$ g cm^{-3}. GJ 9827 c has a mass of $M_c = 1.47^{+0.59}_{-0.58}\,M_\oplus$, radius of $R_c = 1.27^{+0.13}_{-0.13}\,R_\oplus$, and a mean density of $\rho_c = 3.87^{+2.38}_{-1.71}$ g cm^{-3}. For GJ 9827 d we derive $M_d = 2.38^{+0.71}_{-0.69}\,M_\oplus$, $R_d = 2.09^{+0.22}_{-0.21}\,R_\oplus$, and $\rho_d = 1.42^{+0.75}_{-0.52}$ g cm^{-3}.

Conclusions. GJ 9827 is one of the few known transiting planetary systems for which the masses of all planets have been determined with a precision better than 30%. This system is particularly interesting because all three planets are close to the limit between super-Earths and mini-Neptunes. We also find that the planetary bulk compositions are compatible with a scenario where all three planets formed with similar core/atmosphere compositions, and we speculate that while GJ 9827 b and GJ 9827 c lost their atmospheric envelopes, GJ 9827 d maintained its atmosphere, owing to the much lower stellar irradiation. This makes GJ 9827 one of the very few systems where the dynamical evolution and the atmospheric escape can be studied in detail for all planets, helping us to understand how compact systems form and evolve.

Key words. Planetary systems – Techniques: high angular resolution – Techniques: photometric – Techniques: radial velocities – Stars: abundances – Stars: individual GJ 9827

1. Introduction

Systems containing multiple planets have drawn much attention because they have frequently been seen as potential Solar System analogues. However, none of the systems discovered so far resembles ours. The vast majority of multi-planet systems identified by the NASAs *Kepler* space mission contains super-Earths ($1 \le R_p \le 2\,R_\oplus$) and mini-Neptunes ($2 \le R_p \le 4\,R_\oplus$) in tightly packed configurations, with orbits smaller than the orbit of Mercury (Winn and Fabrycky 2015).

Compact systems containing planets of different sizes and masses are the best test beds to constrain planetary formation mechanisms, since all planets have formed under the same initial conditions. The short orbital period increases the geometric probability to see the planets transiting their host stars, allowing us to measure the planetary radii. The Doppler reflex motion is larger, enabling the mass determination via radial velocity (RV) measurements using state-of-the-art, high-precision spectrographs. However, although more than 200 systems with three or more planets have been discovered so far, many questions remains unanswered.

How do compact planetary systems form? It has been proposed that planets with short orbital periods might have either formed *in-situ* (Chiang and Laughlin 2013), or at much larger distance from their host star and then moved inwards via type I or type II migration mechanisms (for a review see Baruteau et al. 2014). Once the disk has been dispersed, planets could also migrate through planet-planet scattering (see, e.g., Marzari and Weidenschilling 2002). Explaining the formation of compact systems with *in-situ* formation is however not easy because a lot of material in the inner disk is required in order to form planets. Using an *in-situ* formation model, Hansen and Murray (2013) found that there are roughly 50% more single-planet candidates observed than those produced by any model population.

⋆ Based on observations made with a) the ESO-3.6m telescope at La Silla Observatory under programme ID 099.C-0491 and 0100.C-0808; b) the Italian Telescopio Nazionale Galileo operated on the island of La Palma by the Fundacin Galileo Galilei of the Istituto Nazionale di Astrofisica; c) the Nordic Optical Telescope, operated by the Nordic Optical Telescope Scientific Association at the Observatorio del Roque de los Muchachos.

Table 1: Equatorial coordinates, optical and near-infrared magnitude, and stellar parameters of GJ 9827.

GJ 9827	
RA[1] (J2000.0)	23:27:04.83647
DEC[1] (J2000.0)	-01:17:10.5816
Distance[1] (pc)	30.32 ± 1.62
V-band magnitude[2] (mag)	10.35 ± 0.10
J-band magnitude[3] (mag)	7.984 ± 0.020
Spectral type[4]	K6 V
Effective temperature[5] $T_{\rm eff}$(K)	4219 ± 70
Surface gravity[5] $\log g_\star$(cgs)	4.650 ± 0.050
Iron abundance[5] [Fe/H] (dex)	−0.29 ± 0.12
Mass[5] $M_\star$ ($M_\odot$)	0.650 ± 0.060
Radius[5] $R_\star$ ($R_\odot$)	0.637 ± 0.063
Projected rot. velocity[5] $v \sin i_\star$ (km s^{-1})	1.5 ± 1.0
Microturbulent velocity[6] $v_{\rm mic}$ (km s^{-1})	0.9 (fixed)
Macroturbulent velocity[7] $v_{\rm mac}$ (km s^{-1})	0.5 (fixed)
Interstellar reddening $A_{\rm v}$ (mag)[5]	0.04 ± 0.08

[1] Hipparcos, the New Reduction (van Leeuwen 2007).
[2] (Mumford 1956).
[3] 2MASS (Skrutskie et al. 2006).
[4] Houdebine et al. (2016).
[5] This work.
[6] Bruntt et al. (2010)
[7] Gray (2008)

How can we observationally distinguish between different scenarios? In order to gain insights into the formation of compact systems, we have to understand whether the planets formed at large distance (e.g., beyond the snow-line), or close-in to their host star. It is now well accepted that the composition of a pre-main sequence disk – where planet formation takes place – depends on the radial distance from the host star. The chemical abundance of planets can thus be used to trace their formation. Thiabaud et al. (2015) showed that the C/O ratio is a good tracer to assess whether a given planet formed *in-situ* or not. The Mg/Si and Fe/Si bulk composition ratios are also interesting tracers. In this respect, the discovery that the ultra-short period planet K2-106 b (Guenther et al. 2017) has an iron core containing 80^{+20}_{-30}% of its mass supports the fact that this planet might have formed in a metal rich environment – typically close to the host star, where photophoresis process can separate iron from silicates in the early phase of planet formation (Wurm et al. 2013). On the contrary, if a close-in planet (a $\lessapprox$ 0.1 AU) were found to have a high quantity of water, this would imply that the planet formed beyond the snow-line and then migrated inwards to its current position (Raymond et al. 2008; Lopez 2017).

On the other hand, as pointed out by Izidoro et al. (2017), the period ratio distribution of planets in multi-planet systems can also provide some clues about the formation mechanisms involved. However, using N-body simulations together with a model of gaseous disc, Izidoro et al. (2017) found also that only 50-60% of resonant chains became unstable whereas to match observations at least 75% (and probably 90-95% according to *Kepler* results) must be expected.

In order to address these questions, a well characterized sample of multi-planet systems transiting relatively bright stars, for which planetary radii, masses, and orbital parameters have been determined with high accuracy is needed. The three brightest systems known to host three or more planets for which masses have been determined for all planets, are Kepler-89 (V=12.2 mag, 4 planets), K2-32 (V=12.3 mag, 3 planets), and Kepler-138 (V=12.9 mag, 3 planets). However, for most of the planets in these systems masses are known with a precision of only ∼50% due to the faintness of the host stars.

To increase the sample of compact systems with planetary masses with a precision at least better than 30%, we need to detect brighter systems (V$\lessapprox$12 mag) for which radial velocity (RV) precisions of 1 m s^{-1} can be achieved using state-of-the-art spectrographs during a reasonable amount of telescope time.

Using *K2* time-series photometry from Campaign 12, we have recently discovered that the star GJ 9827 – also known as K2-135 and EPIC 246389858 (Table 1) – hosts three transiting small planets ($R_{\rm p} \lesssim 2\,R_\oplus$) with orbital periods of 1.2, 3.6, and 6.2 days (Niraula et al. 2017; Rodriguez et al. 2018). With a distance of only 30.32 ± 1.62 pc, GJ 9827 is the nearest planetary system detected by *Kepler* and *K2*, and with V=10.35 mag (Table 1) is the brightest system known to host 3 transiting planets.

In this paper, we present the high-precision RV measurements we collected between July and December 2017 to measure the masses of the three small planets transiting GJ 9827. This work is part of the ongoing RV follow-up program of *K2* transiting planets successfully carried out by our consortium `KESPRINT` (see, e.g., Nowak et al. 2017; Fridlund et al. 2017; Gandolfi et al. 2017; Barragán et al. 2017; Dai et al. 2017; Guenther et al. 2017).

2. Ground based follow-up observations

2.1. High-spacial resolution

We conducted speckle imaging observations of the host star with the WIYN 3.5-m telescope and the NASA Exoplanet Star and Speckle Imager (NESSI, Scott et al. (2016), Scott et al., in prep.). The observations were conducted at 562nm and 832nm simultaneously, and the data were collected and reduced following the procedures described by Howell et al. (2011). The resulting reconstructed images of the host star are 4.6″ × 4.6″, with a resolution close to the diffraction limit of the telescope. We did not detect any secondary sources in the reconstructed images, and we produced 5σ detection limits from the reconstructed images using a series of concentric annuli (see Figure 1).

2.2. FIES

We collected 7 RV measurements of GJ 9827 with the FIbre-fed Echelle Spectrograph (FIES; Frandsen and Lindberg 1999; Telting et al. 2014) on the 2.56 m Nordic Optical Telescope (NOT) at the Observatorio del Roque de los Muchachos, La Palma (Spain). The data have already been presented in Niraula et al. (2017). We refer the reader to this work for a description of the observational strategy and data reduction. For the sake of completeness, we report the RV measurements in Table .1.

Table 2: Spectroscopic parameters of GJ 9827 as derived from the co-added HARPS (top) and HARPS-N (bottom) spectra using the two methods described in Sect 3.1.

Method	$T_{\rm eff}$ (K)	$\log g_\star$ (cgs)	[Fe/H] (dex)	$R_\star$ ($R_\odot$)	$v \sin i_\star$ ($\mathrm{km\,s^{-1}}$)
HARPS					
SpecMatch-Emp	4203±70	.....	−0.27±0.12	0.648±0.065	.....
SME 5.2.2	4204±90	4.52±0.20	−0.50±0.20	.....	1.5±1.0
HARPS-N					
SpecMatch-Emp	4234±70	.....	−0.30±0.12	0.651±0.065	.....
SME 5.2.2	4236±90	4.44±0.20	−0.53±0.20	.....	1.5±1.0

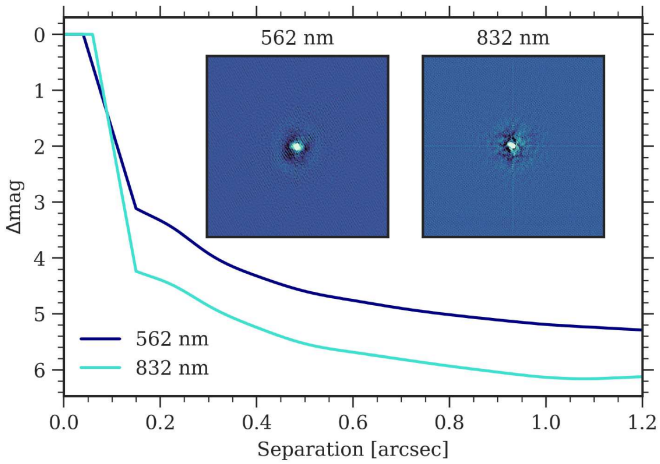

Fig. 1: Reconstructed images from WIYN/NESSI speckle interferometry and the resulting 5σ contrast curves. The inset images are $4.6'' \times 4.6''$ and northeast is up and to the left.

2.3. HARPS and HARPS-N

We obtained 35 high-precision RVs with the HARPS spectrograph (Mayor et al. 2003) on the 3.6 m ESO telescope at La Silla Observatory under programs 099.C-0491 and 0100.C-0808, and 23 RV measurements with the HARPS-N spectrograph (Cosentino et al. 2012) on the 3.58 m Telescopio Nazionale Galileo (TNG) at La Palma under programs OPT17A_64 and A36TAC_12. The HARPS spectra were gathered from August 19 to October 24 2017 UT, and the HARPS-N spectra from July 29 to December 9 2017 UT. Both spectrographs have a resolving power of $R = \lambda/\Delta\lambda \approx 115\,000$. HARPS covers the wavelength region from 3830 Å to 6900 Å, whereas HARPS-N from 3780 Å to 6910 Å. We used the second fiber of both instruments to monitor the sky background. All calibration frames were taken using the HARPS and HARPS-N standard procedures. The spectra were reduced and extracted using the dedicated data reduction software (DRS). The RVs were measured by cross-correlating the Echelle orders of the observed spectra with a K5 numerical mask (Baranne et al. 1996; Pepe et al. 2002) and by fitting a Gaussian function to the average cross-correlation function (CCF). The DRS provides also the absolute RV, the bisector span (BIS) and full-width at half maximum (FWHM) of the CCF, and the Ca II S-index activity indicator. We list the HARPS and HARPS-N measurements in Tables .2 and .3.

3. Properties of the host star

3.1. Spectral analysis

In our previous paper (Niraula et al. 2017), we derived the spectroscopic parameters of GJ 9827 using the co-added FIES spectrum, which has a S/N ratio of ∼150 per pixel at 5500 Å. As part of the analysis presented in this work, we refined the spectroscopic properties of the host star using the combined HARPS and HARPS-N spectra, taking advantage of their higher resolving power ($R \approx 115\,000$) and S/N ratio (∼440 and 400, respectively). The spectral analysis was performed following the same methods used in (Niraula et al. 2017), which, for the sake of completeness, are briefly described in the next paragraphs.

We used `SpecMatch-Emp` (Yee et al. 2017), a software suite that utilizes hundreds of Keck/HIRES template spectra of stars whose parameters have been accurately measured via interferometry, asteroseismology, spectral synthesis, and spectrophotometry. The fit is performed in the spectral region 5000-5900 Å. The output parameters of `SpecMatch-Emp`, namely, the effective temperature $T_{\rm eff}$, stellar radius $R_\star$, and iron abundance [Fe/H], are derived by interpolating those of the best matching library stars. Following Hirano et al. (2017), prior to our analysis we reformatted the co-added HARPS and HARPS-N spectra so that they have the same spectral format as Keck/HIRES.

We also analyzed the HARPS and HARPS-N data with the spectral analysis package `SME` Valenti and Piskunov (1996); Valenti and Fischer (2005). `SME` calculates synthetic spectra from model atmospheres and fits them to the observed spectrum using a χ^2 minimizing procedure. The analysis was carried out with the non-LTE version of the code (5.2.2) and `ATLAS 12` model atmospheres (Kurucz 2013). Following the calibration equation for Sun-like stars from Bruntt et al. (2010), we fixed the microturbulent velocity to $v_{\rm mic} = 0.9\,\mathrm{km\,s^{-1}}$. The macroturbulent velocity $v_{\rm mac}$ was assumed to be $0.5\,\mathrm{km\,s^{-1}}$(Gray 2008). Following Fuhrmann et al. (1993, 1994), the line wings of the H_α and H_β lines were fitted to determine the effective temperature $T_{\rm eff}$. The surface gravity $\log g_\star$ was measured from the wings of the Ca I λ6102, 6122, 6162 Å triplet, and the Ca I λ6439 Å line. The iron [Fe/H] and calcium [Ca/H] abundance, as well as the projected rotational velocity $v \sin i_\star$ were derived fitting the profile of clean and unblended narrow lines in the spectral region between 6100 and 6500 Å. The analysis was finally checked with the Na doublet λ5889 and 5896 Å.

We summarize our results in Table 2. The effective temperatures derived by `SpecMatch-Emp` and `SME` agree well within the nominal error bars. As for the iron abundance, the two methods provide consistent results within $\sim 2\sigma$. It is worth noting that the error bars calculated by `SME` are larger than those given

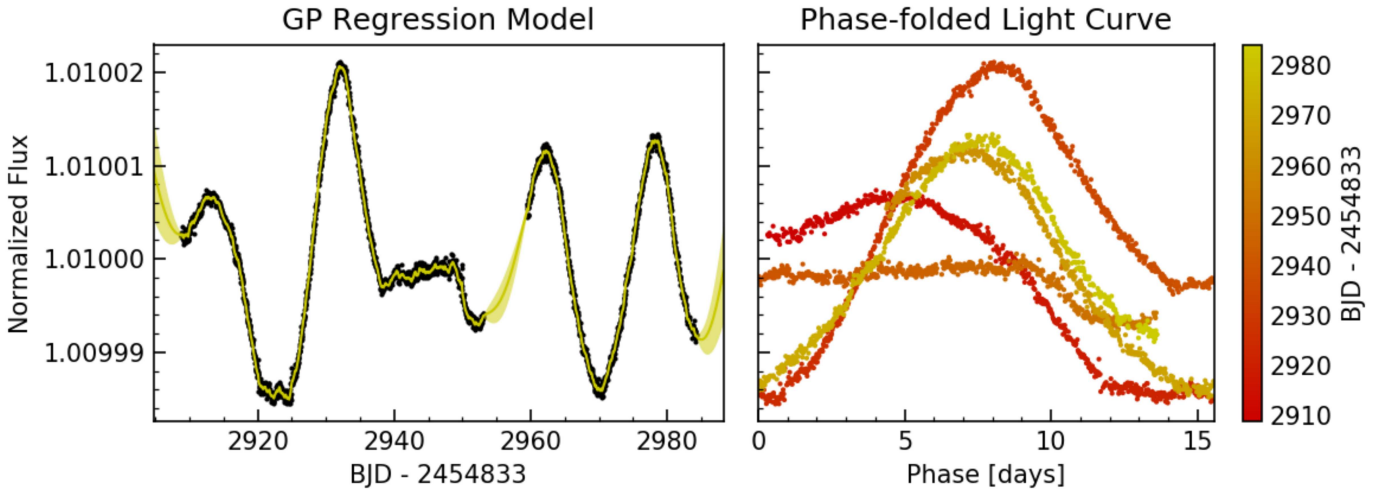

Fig. 2: *Left panel*: Gaussian process regression model applied to the detrended K2 light curve. Black points are *K2* light curve, yellow band is the Gaussian model. *Right panel*: *K2* detrended light curve phase-folded to the $P_{\rm rot/2}$ stellar rotational period.

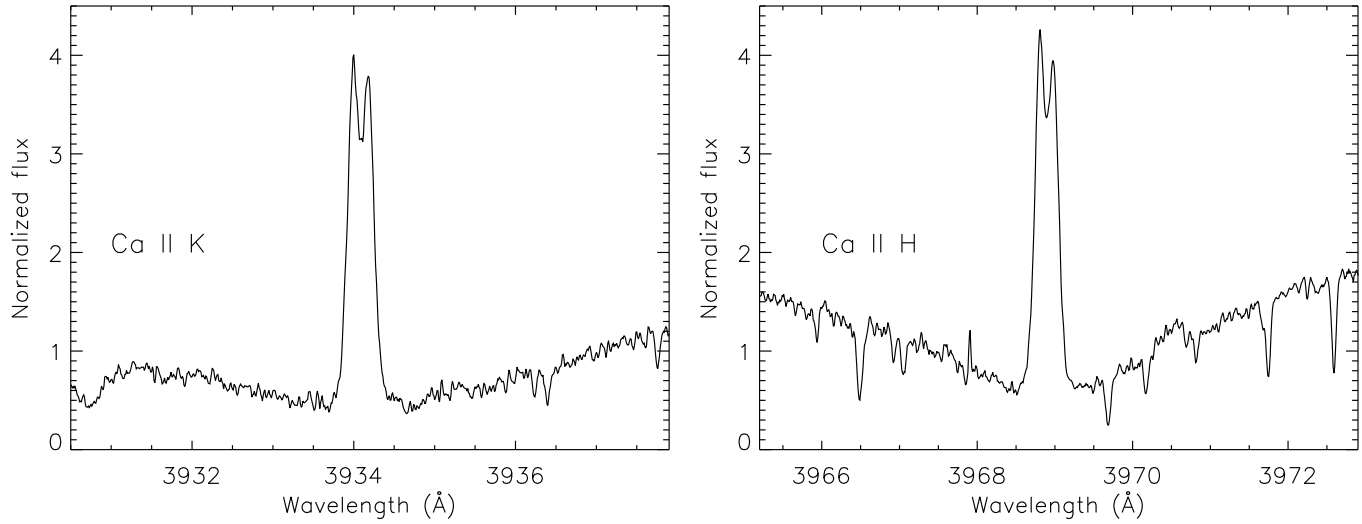

Fig. 3: Cores of the Ca II H & K lines of GJ 9827 as observed with HARPS.

by `SpecMatch-Emp`, owing to the physical uncertainties of model atmospheres of cool stars ($T_{\rm eff} < 4500$ K). We therefore adopted the effective temperature and iron abundance measured by `SpecMatch-Emp` and averaged the estimates from the HARPS and HARPS-N spectra. For the projected rotational velocity $v \sin i_\star$, we adopted the value determined with `SME`. We found $T_{\rm eff} = 4219 \pm 70$ K, [Fe/H] $= -0.29 \pm 0.12$ (cgs), and $v \sin i_\star = 1.5 \pm 1.0$ km s^{-1} (Table 1). The stellar radius and surface gravity were determined using a different method, as described in the following section.

3.2. Stellar radius and mass

We built the spectral energy distribution of GJ 9827 using the Johnson B and V (Mumford 1956) and 2MASS JHKs (Skrutskie et al. 2006) magnitudes. Following the method described in Gandolfi et al. (2008), we measured the interstellar redding ($A_{\rm v}$) along the line of sight to the star and found $A_{\rm v} = 0.04 \pm 0.08$ mag (Table 1), which is consistent with zero, as expected given the proximity of GJ 9827. We note that our result agrees with previous findings from McDonald et al. (2017) and Gontcharov and Mosenkov (2018), confirming that the star suffers a negligible reddening.

We derived the stellar radius $R_\star$ by combining the Hipparcos' distance d $= 30.32 \pm 1.62$ pc (van Leeuwen 2007), with the apparent magnitude V $= 10.35 \pm 0.10$ mag (Mumford 1956) and our effective temperature estimate $T_{\rm eff} = 4219 \pm 70$ K (Sect. 3.1). Assuming no reddening ($A_{\rm v}$=0 mag), we found a stellar radius of $R_\star = 0.637 \pm 0.063\, R_\odot$, which agrees with the spectroscopic radius derived using `SpecMatch-Emp` (cfr. Table 2).

We finally converted $T_{\rm eff}$, $R_\star$, and [Fe/H] into stellar mass $M_\star$ and surface gravity $\log g_\star$ using Mann et al. (2015)'s empirical equations coupled to Monte Carlo simulations. We found that GJ 9827 has a mass of $M_\star = 0.650 \pm 0.060\, M_\odot$ and a surface gravity of $\log g_\star = 4.650 \pm 0.050$ (cgs), which agrees with the spectroscopic gravity derived using `SME` (cfr. Table 2). According to our analysis performed with `SpecMatch-Emp`, the three stars[1] whose spectra best match the HARPS and HARPS-N spectra of GJ 9827 have masses between 0.62 and 0.64 $M_\odot$,

[1] HIP 12493, HIP 97051, and HIP 15095.

confirming our results. The derived stellar mass and radius are are given in Table 1.

3.3. Stellar activity and rotation period

The *K2* light curve of GJ 9827 displays a quasi-periodic photometric variability with a peak-to-peak amplitude of about 0.4 % (Fig. 2, left panel). Given the late spectral type of the star (K6 V), the observed photometric variation is very likely caused by active regions (sun-like spots and plages) crossing the visible stellar hemisphere as the star rotates about its axis. This is corroborated by the detection of emission components in the cores of the Ca II H & K lines (Fig. 3), from which we measured an average S-index of 0.677 ± 0.034 and 0.739 ± 0.021 using the HARPS and HARPS-N spectra, respectively.

Applying the auto cross-correlation technique to the *K2* light curve, (Niraula et al. 2017) and (Rodriguez et al. 2018) found that the rotation period $P_{\rm rot}$ of the star is either ∼17 or 30 days. We note that the ratio between the two measurements is close to 2, suggesting that the first might be the harmonic of the second. A visual inspection of the *K2* light curve reveals that there are two dips whose minima occur at $\mathrm{BJD_{TBD}} - 2454833 \approx 2922$ and 2971 days, with a duration of ∼20 and 16 days, respectively (Fig. 2, left panel). If the observed dips are caused by active regions crossing the visible hemisphere of GJ 9827, the rotation period is likely longer than 17 days, suggesting that $P_{\rm rot}$ might be twice as long. A Gaussian process (GP) analysis of the *K2* light curve (Sect. 5.2) shows a posterior bimodal distribution with rotational periods peaking at 15.1±1.6 and 30.7±1.4 days, showing just a minimal difference between both. Thus GP analysis does not provide a conclusive result about the rotation period of the star.

4. Frequency analysis of the HARPS and HARPS-N data

The presence of active regions coupled to stellar rotation is expected to induce periodic and quasi-periodic RV signals at the stellar rotation frequency and its harmonics (see, e.g., Hatzes et al. 2010; Haywood 2015). Using the code SOAP2 (Dumusque et al. 2014), we estimated the amplitude of the activity-induced RV signal – the so-called activity-induced RV *jitter* – from the properties of the star, namely, its effective temperature, radius, rotation period, and photometric variability. We found that the predicted semi-amplitude of the RV jitter is $\sim 5\,\mathrm{m\,s^{-1}}$. Given the precision of most of our measurements ($\sim 1\,\mathrm{m\,s^{-1}}$), RV jitter is expected to be detected in our data-set.

We searched our Doppler time-series data for periodic signals associated with stellar activity by performing a frequency analysis of the RV measurements and activity indicators. For this purpose, we used only the HARPS and HARPS-N data because of the higher precision of the two data-sets. On epoch BJD=2458046, we purposely observed GJ 9827 with both HARPS and HARPS-N nearly simultaneously (within less than 25 minutes) and used the two sets of measurements to estimate the RV, FWHM, BIS, and S-index offsets between the two instruments. We stress that these offsets have only been used to perform the periodogram analysis of the joint data.

Figure 4 displays the generalized Lomb-Scargle periodograms (GLS; Zechmeister and Kürster 2009) of the combined HARPS and HARPS-N data following the correction for instrument offset. From top to bottom, we show the periodograms of the combined HARPS and HARPS-N RVs, the RV residuals after subtracting the stellar activity signal assumed to be a Fourier component at $2f_{\rm rot}$ (Sect. 5), the RV residuals after subtracting the 3 planetary signals, the CCF bisector span (BIS), the CCF FWHM, the S-index, and the window function. Periodograms are displayed for two frequencies ranges encompassing the planetary and stellar signals. The vertical dotted lines mark the orbital frequencies of planet b, c, and d, as well as the stellar rotational frequency and its first 2 harmonics. The horizontal dotted lines mark the false alarm probabilities (FAP) of 0.1% derived using the bootstrap method described in (Kuerster et al. 1997).

There are several important features to highlight in Figure 4. The periodogram of the RV data shows peaks at the stellar rotational frequency and its harmonics (first row). The highest peak is found at about twice the rotation frequency with a semi-amplitude of $\sim 3\,\mathrm{m\,s^{-1}}$, in fairly good agreement with the value predicted by SOAP2 ($\sim 5\,\mathrm{m\,s^{-1}}$). Whereas the signals at the rotation frequency and its harmonics have a FAP > 0.1 in the periodogram of the RV data (first panel), their significances increase with the FAP ≤ 0.1 once the 3 planetary signals are subtracted from the time-series (third row). The periodograms of the CCF FWHM and S-index show also significant peaks (FAP ≤ 0.1) whose frequencies are close to the stellar rotation frequency and its first harmonics, confirming that these signals are due to activity.

The presence of two/three active regions separated by ∼180/120 degrees in longitude might account for the first and second harmonic of the fundamental rotation frequency. It's worth noting that the periodogram of the window function (lower row) shows a peak at 0.0342 c/d (∼29 days; red arrow), reflecting the fact that our follow-up was carried out around new moon to avoid the contamination from the scattered Sun light. Since the sampling frequency is very close to the rotation frequency of the star, we acknowledge that the peaks associated to the rotation frequency and its harmonics might also arise from aliasing effects.

The periodogram of the RV residuals after subtracting the activity signal at $P_{\rm rot}/2$ (Sect. 5) shows a significant peak (FAP ≤ 0.1) at the orbital frequency of GJ 9827 b (Figure 4, second row). We conclude that the signal of the inner planet is clearly present in our RV data and that we would have been able to detect GJ 9827 b even in the absence of the K2 transit photometry.

5. Data analysis

We modeled the *K2* and RV data using two different techniques, as described in the following two sub-sections.

5.1. Pyaneti analysis

We performed the joint analysis to the photometric and RV data with the code `pyaneti` (Barragán et al. 2017), which explores the parameter space using a Markov chain Monte Carlo (MCMC) algorithm. We fitted Keplerian orbits to the RV data and used the limb-darkened quadratic transit model by Mandel and Agol (2002) for the *K2* transit light curves. In order to account for the *Kepler* long-cadence acquisition, we supersampled the transit models using 10 subsamples per *K2* exposure (Kipping 2010). The fitted parameters and likelihood are similar to those used in previous analyses performed with `pyaneti` and described, e.g., in Barragán et al. (2016); Gandolfi et al. (2017).

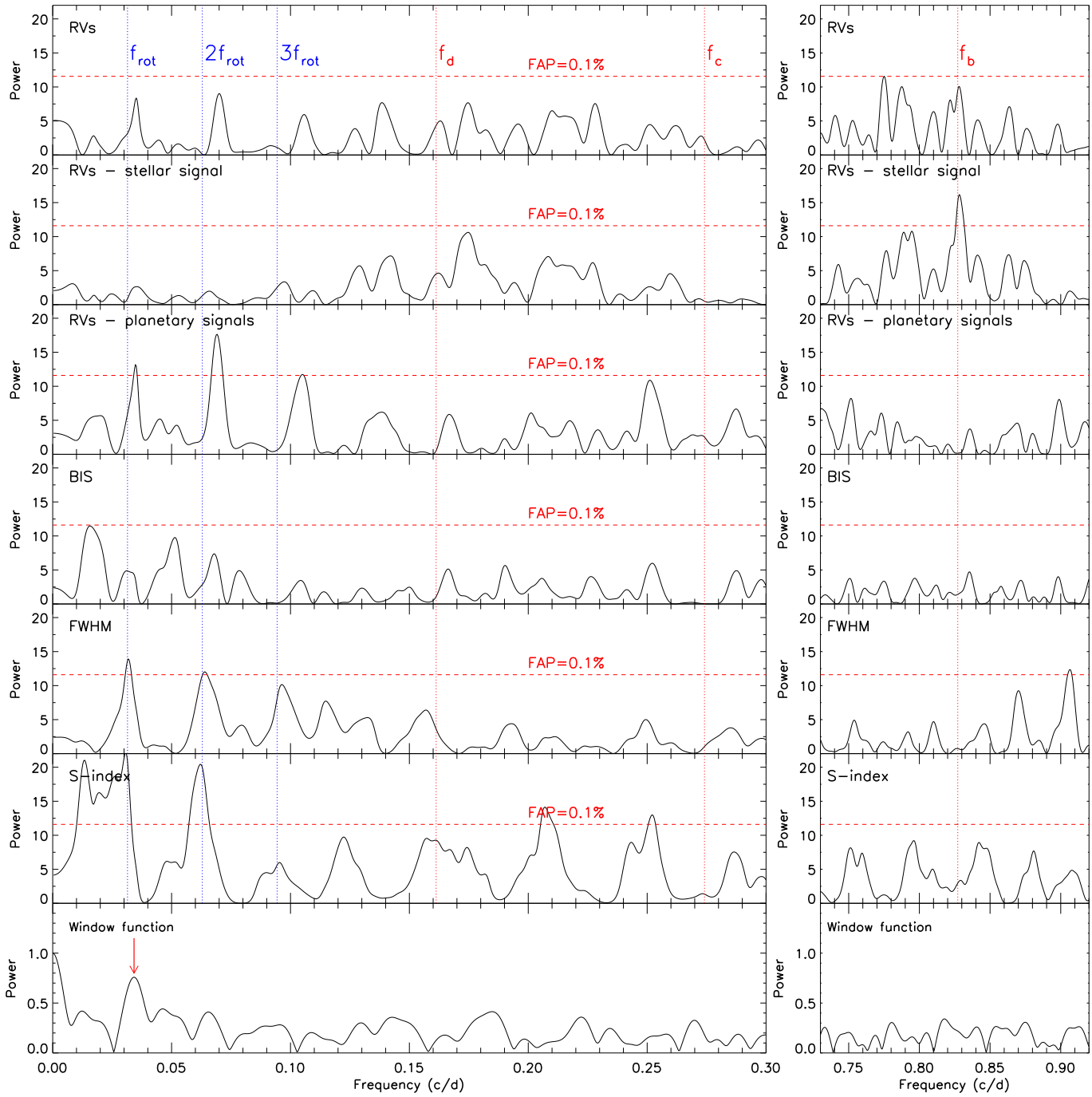

Fig. 4: Generalized Lomb-Scargle periodograms of the combined HARPS and HARPS-N datasets. The right and left columns cover two frequency ranges encompassing the 3 planetary signals (dotted vertical red lines), as well as the stellar rotation frequency and its first 2 harmonics (dotted vertical blue lines). From top to bottom: the RV data, the RV residuals after subtracting the signals of the 3 transiting planets, the RV residuals after subtracting the stellar activity signal, the BIS and FWHM of the CCF, and the window function. The dashed horizontal red lines mark the 0.1 % false alarm probabilities as derived using the bootstrap technique. The red arrow in the lower panel marks the peak discussed in the main text.

We fitted for a transit and a RV signal for each of the three planets. We sampled for $\rho_\star^{1/3}$ and recovered the scaled semi-major axis ($a_p/R_\star$) of the three planets using Kepler's third law. We used uniform informative priors for all the parameters, except for the limb darkening coefficients for which we set Gaussian priors as described in Niraula et al. (2017).

As presented in the previous section, the RV data of GJ 9827 shows activity-induced jitter at the stellar rotation frequency and its harmonics, with a semi-amplitude of ~3 m s^{-1}. The light curve of GJ 9827 (Fig. 2, left panel) suggests that the evolution time scale of active regions is longer than the *K2* observations (~80 days). Since our FIES, HARPS, and HARPS-N RV follow-up covers ~140 days, we can model the RV jitter using coherent sinusoidal signals at the stellar rotation frequency and its

harmonics, similarly to the work described in, e.g., Pepe et al. (2013) and Barragán et al. (2017).

In order to check which Fourier components at the rotation frequency and its harmonics can better describe the activity signal, we tested different RV models. The first model (3P) includes only the three planetary signals. The second model (3P+P_{rot}) is obtained from 3P by adding a sinusoidal signal at the rotation period of the star (P_{rot}~30 days). The third model called 3P+$P_{rot}/2$ includes three Keplerians and a sinusoidal signal at half the rotation period (~15 days). We also tested a model where two sinusoidal signals at both P_{rot} and $P_{rot}/2$ were included. Since the stellar rotation period is not well constrained, we set uniform priors in the ranges $[P_{rot}-2 : P_{rot}+2]$ and $[P_{rot/2}-1 : P_{rot/2}+1]$.

Table 3 summarizes out the results of our test, showing the goodness of the fit for each model. With the lowest Bayesian information criteria (BIC), the preferred model is 3P+$P_{rot}/2$ (3 planets plus one sinusoidal signal at ~15 days). Table 3 shows also that the semi-amplitudes of the three planetary signals do not change significantly when considering different models, providing evidence that the Doppler motion induced by the three planets is present in our RV data-set and does not depend on the Fourier components used to model the activity-induced RV signal.

We performed a final joint analysis assuming that the RV data are described by the 3P+$P_{rot/2}$ model. For the phase, amplitude, and period of the activity signal we adopted uniform priors. We included a jitter term for each spectrograph to account for additional instrumental noise not included in the nominal RV error bars and/or imperfect treatment of the various sources of RV variations. Since GJ 9827 hosts a short-period multi-planetary system, we assumed tidal circularization of the orbits and fixed $e = 0$ for all three planets (Van Eylen and Albrecht 2015). We explored the parameter space with 500 Markov chains initialized at random positions in the parameter space. Once all chains converged, we ran 5000 iterations more. We used a thin factor of 10 to generate a posterior distribution of 250,000 independent points for each parameter. We used the posterior distribution of each parameter to infer their values and its uncertainty given the median and the 68.3% credible interval. The final fits are shown in Fig.5 and Fig. 6; parameter estimates are summarized in Table 5.

5.2. Gaussian process

We also experimented with Gaussian Process (GP) to model the correlated RV noise associated with stellar activity. GP models stochastic processes with covariance matrices whose elements are generated by user-chosen kernel functions. GP regression has been successfully used to deal with the correlated stellar noise of the radial velocity datasets of several exoplanetary systems including CoRoT-7, Kepler-78, Kepler-21, and K2-141 (Haywood et al. 2014; Grunblatt et al. 2015; López-Morales et al. 2016; Barragán et al. 2018).

Our GP model was described in detail by Dai et al. (2017). Briefly, we adopted a quasi-periodic kernel with the following hyperparameters: the covariance amplitude h, the correlation timescale τ, the period of the covariance T, and Γ which specifies the relative contribution between the squared exponential and periodic part of the kernel. For each of the transiting planets in GJ 9827, we included a circular Keplerian signal specified by the RV semi-amplitude K, the orbital period P_{orb} and the time of conjunction t_c. For each of spectrographs, we included a jitter parameter σ and a systematic offset γ. We imposed Gaussian priors on P_{orb} and t_c with those derived from *K2* transit modeling (Sect.5.1). For the scale parameters h, K, and the jitter parameters we imposed Jeffreys priors. We imposed uniform priors on the systematic offsets γ_{HARPS}, $\gamma_{HARPS\text{-}N}$, and γ_{FIES}. Finally, for the hyperparameters τ, Γ, and T we imposed priors that were derived from a GP regression of the observed *K2* light curve, as described below.

When coupled with stellar rotation, active regions on the host star give rise to quasi-periodic variations in both the measured RV and the flux variation. Given their similar physical origin, one would expect that GP with similar hyperparameters are able to describe the quasi-periodic variations seen in both datasets. Since the *K2* light curve was measured with higher precision and sampling rate than our RV dataset, we trained our GP model on the *K2* light curve. The resultant constrains on the hyperparameters were then used as priors when we analyzed the RV dataset. We adopted the covariance matrix and the likelihood function described by Dai et al. (2017). We first located the maximum likelihood solution using the Nelder-Mead algorithm implemented in the `Python` package `scipy`. We then sampled the posterior distribution using the affine-invariant MCMC implemented in the code `emcee` (Foreman-Mackey et al. 2013). We started 100 walkers near the maximum likelihood solution. We stopped after running the walkers for 5000 links. We checked for convergence by calculating the Gelman-Rubin statistics which dropped below 1.03 indicating adequate convergence. We report the various parameters using the median and 16%-84% percentiles of the posterior distribution. The hyperparameters were constrained to be $\tau = 6.1^{+4.0}_{-2.3}$ days, $T = 15.1 \pm 1.6$ days and $\Gamma = 0.77^{+0.47}_{-0.29}$. These served as priors in the subsequent GP analysis of the RV data. The GP model of the *K2* light curve is shown in Fig. 2.

In the analysis of the RV dataset with GP regression, we first found the maximum likelihood solution and sampled the parameter posterior distribution with MCMC using the same procedure as described above. The RV semi-amplitude for planet b, $K_b = 3.41 \pm 0.53$ m s^{-1} was detected to a high significance. The RV signal of planet c was not securely detected in GP model. We therefore report the upper limit of $K_c < 1.1$ m s^{-1} at a 95% confidence level. Finally, the RV signal of the outer planet was detected but with less confidence than the inner planet. We report a value of $K_d = 1.06 \pm 0.52$ m s^{-1}. The amplitude of the correlated stellar noise is $h_{rv} = 2.30^{+0.97}_{-0.66}$ m s^{-1}. All this values are in perfect agreement with the ones derived in previous section. Fig. 7 shows the FIES, HARPS, and HARPS-N RVs of GJ 9827 and the GP model. The planet parameter estimates are summarized in Table 5.

Given the good agreement between the results provided by the two methods and the fact that GP analysis provides only upper limit to the mass of the second planet, we adopted the values obtained with `Pyaneti`.

6. Discussion

We determined masses, radii, and densities of the three planets known to transit GJ 9827. We found that GJ 9827 b has a mass of $M_b = 3.74^{+0.50}_{-0.48} M_\oplus$ and a radius of $R_b = 1.62^{+0.17}_{-0.16} R_\oplus$, yielding a mean density of $\rho_b = 4.81^{+1.97}_{-1.33}$ g cm^{-3}. GJ 9827 c has a mass of $M_c = 1.47^{+0.59}_{-0.58} M_\oplus$, radius of $R_c = 1.27^{+0.13}_{-0.13} R_\oplus$, and a mean density of $\rho_c = 3.87^{+2.38}_{-1.71}$ g cm^{-3}. For GJ 9827 d we derived $M_d = 2.38^{+0.71}_{-0.69} M_\oplus$, $R_d = 2.09^{+0.22}_{-0.21} R_\oplus$, and $\rho_d = 1.42^{+0.75}_{-0.52}$ g cm^{-3}. Figure 8 shows the planetary masses as a function of the host star's visual magnitudes for systems known to host at least three

Table 3: Model comparison.

Model	K_b (m s^{-1})	K_c (m s^{-1})	K_d (m s^{-1})	K_{rot} (m s^{-1})	$K_{rot/2}$ (m s^{-1})	χ^2/dof	BIC
3P	2.86 ± 0.28	0.80 ± 0.24	1.26 ± 0.25	0	0	2.8	-500
3P + P_{rot}	2.96 ± 0.30	1.11 ± 0.27	0.99 ± 0.26	5.68 ± 0.84	0	1.9	-539
3P + $P_{rot/2}$	3.01 ± 0.28	0.85 ± 0.27	1.16 ± 0.27	0	3.18 ± 0.38	1.4	-564
3P + P_{rot} + $P_{rot/2}$	2.98 ± 0.31	0.82 ± 0.27	1.25 ± 0.30	$0.64^{+1.10}_{-0.47}$	3.27 ± 0.50	1.7	-488

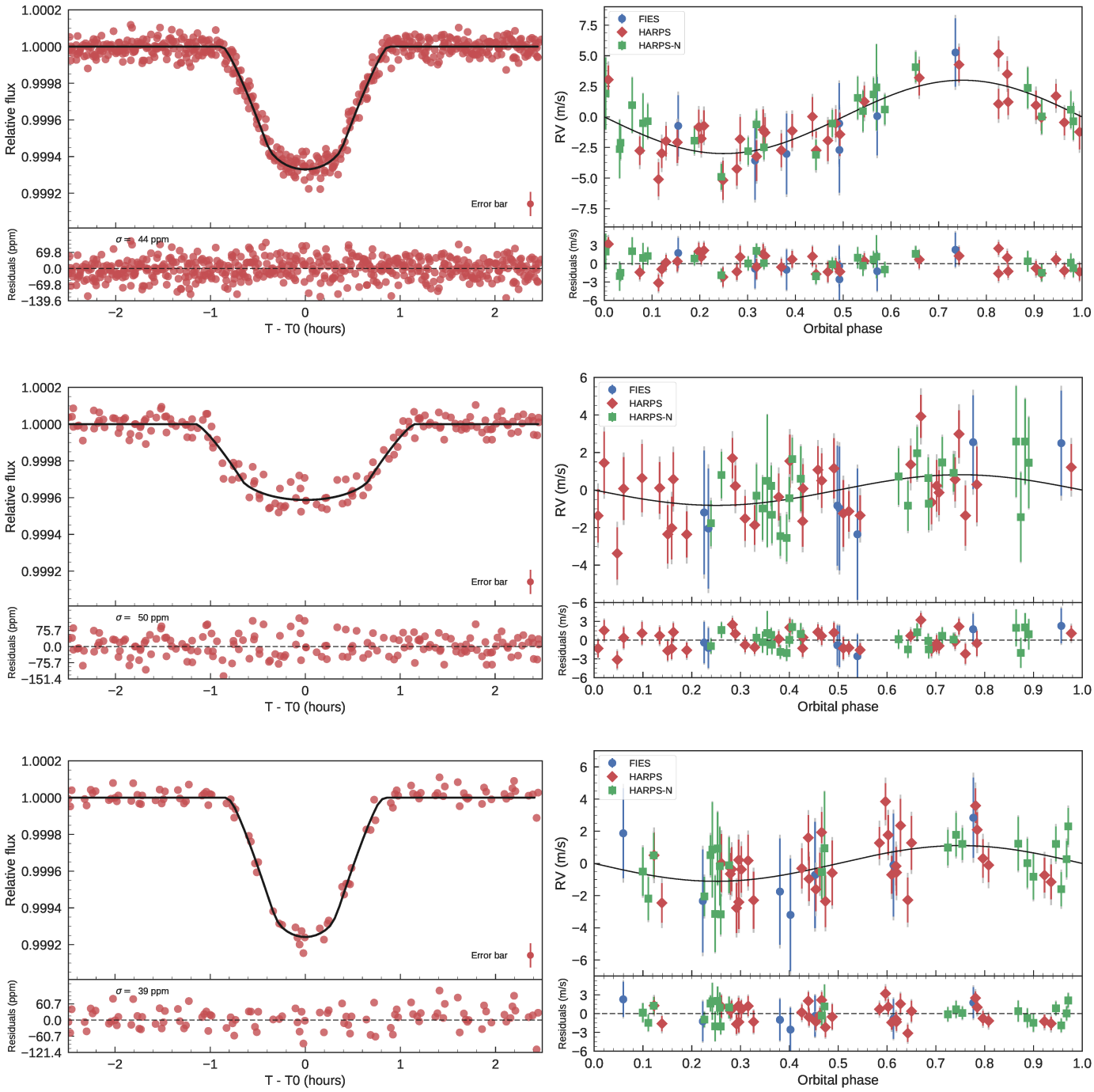

Fig. 5: From top to bottom and left to right: transit fit and phase-folded RV curve of GJ 9827 b, GJ 9827 c, GJ 9827 d after removing the activity signal from the star and the signals from the other planets. The gray error bars account for additional instrumental noise and/or imperfect treatment of the various sources of RV variations.

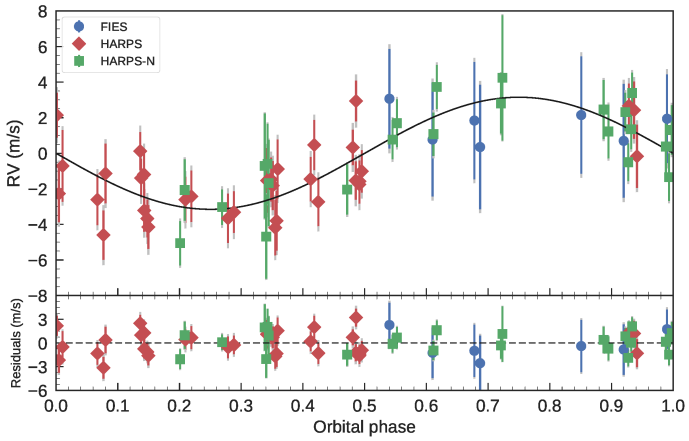

Fig. 6: RV curve of GJ 9827 phase-folded to the first harmonic of the stellar rotation period ($P_{\rm rot}/2 = 15.1$ days) after removing the signals of the three transiting planets.

planets. GJ 9827 is the brightest (V=10.35 mag) transiting multi-planet system for which the masses of all planets have been measured.

In the next sub-sections we will address the following questions. What type of planets are GJ 9827 b, c, and d, and how well can we constrain their evolutionary history?

6.1. Planets composition

To address these questions we can rely on the recent discovery of the existence of a bimodal distribution of planetary radii described by Fulton et al. (2017) and Van Eylen et al. (2017). According to these works, there is a clear distinction between two different families of planets: super-Earths whose radius distribution peaks at $R_{\rm p} \sim 1.5\,R_{\oplus}$, and sub-Neptunes whose radius distribution peaks at $R_{\rm p} \sim 2.5\,R_{\oplus}$, separated by a dearth planet valley. The characteristics of this frontier (negative slope, dependence with period/incident flux) can be explained with photoevaporation of planetary atmospheres due to XUV radiation from the host stars.

GJ 9827 hosts a canonical terrestrial planet, GJ 9827 c, and two planets close to the dearth valley but from different sides: the super-Earth GJ 9827 b and the sub-Neptune GJ 9827 d. Fig. 9 shows the position of the three planets in the mass-radius diagram along with the Zeng et al. (2016)'s theoretical models for different internal compositions. Planets b and c may have rocky nuclei with traces of lighter elements. Given its radius, planet d is likely surrounded by a large gaseous H/He-rich envelope. Since the innermost planets lie on the same isocomposition line of ~80%$MgSiO_3$-20%H_2O (Fig. 9), we can speculate that the outer planet might have a similar composition too. According to Wolfgang and Lopez (2015), the atmosphere of GJ 9827 d would account for up to only ~1% of the total mass, yielding to a thickness of $\sim 0.6\,R_{\oplus}$, i.e., ~30% of the planet's radius.

6.2. Planets formation

Based on the low abundance of resonant orbits among *Kepler* multi-planet systems, Izidoro et al. (2017) found that the instability rate of resonant chains is roughly 95%. This means that GJ 9827 belongs to the exclusive group of only 5% of systems showing resonances. However, how this system came up to this configuration? To place GJ 9827 in context, we show all transiting triple systems known so far in Table 4, along with the ratios between the periods of their planets[2]. A plethora of these systems have 1:2 or 2:3 period ratios. These resonances have been theoretically predicted by Wang and Ji (2017), where type I migration plays a central role. Remarkably, the triple resonance 1:2:4 appears frequently where close-in terrestrial planets form driven by migration mechanisms (Sun et al. 2017; Wang and Ji 2017). However, the resonant chain of the GJ 9827 planetary system (1:3:5) is far more complex, indicating that possibly formation mechanism other than migration could be at play.

How did GJ 9827 reach the 1:3:5 resonance? According to Izidoro et al. (2017), during planet formation, when the first embryo reaches the inner edge of the disk, its migration is stopped by the planet disk-edge interaction (Masset et al. 2006) and other embryos migrate into a resonant chain. If this formation scenario is correct, several features would still be codified in the orbital eccentricity of the planets. As Van Eylen and Albrecht (2015) demonstrated, from precise photometry (like the one gathered by *K2* or by the upcoming space-telescope CHEOPS (Broeg et al. 2013)) and using accurate asteroseismic density measurements (as those from the future PLATO mission (Rauer 2017)) the eccentricity of close-in planets could be precisely measured.

On the other hand, the masses of the three planets amount to a total mass of only $7.6 \pm 1.8\,M_{\oplus}$ (less than half the mass of Neptune), a quantity that could be compatible with an *in-situ* formation scenario. Chiang and Laughlin (2013) demonstrated that *in-situ* formation in the minimum-mass extrasolar nebula is fast, efficient, and can reproduce many of the observed properties of close-in super-Earths. Therefore, if we could demonstrate that the three planets orbiting GJ 9827 have formed *in-situ* many information would be inferred about the primordial formation scenario of the system. One observationally testable property of close-in super-Earths mentioned by Chiang and Laughlin (2013) is that they retain their primordial hydrogen envelopes. Additionally, if these planets did not migrate from the behind the snow-line and formed close to the host star they should not show any water features on their atmospheres.

Table 4: Triple transiting systems with measured masses

System	Resonance	M_1 ($M_{\oplus}$)	M_2 ($M_{\oplus}$)	M_3 ($M_{\oplus}$)
Kepler-18	1:2:4	6.99	17.16	16.53
Kepler-30	1:2:4	11.44	638.83	23.20
Kepler-51	1:2:3	2.22	4.13	7.63
Kepler-60	3:4:5	4.19	3.85	4.16
Kepler-138	2:3:4	0.07	1.97	0.64
Kepler-289	1:2:4	7.31	4.13	133.49
K2-32	1:2:3	16.50	12.10	10.30
GJ 9827	1:3:5	3.72	1.44	2.72

[1] Data taken on 2018 Feb 1st, from NASA Exoplanet Archive: https://exoplanetarchive.ipac.caltech.edu

6.3. Planets atmosphere

The fate of the atmosphere of an exoplanet strongly depends on the incident flux per surface unit due to photoevaporation pro-

[2] Source: NASA Exoplanet Archive as of 1 February 2018.

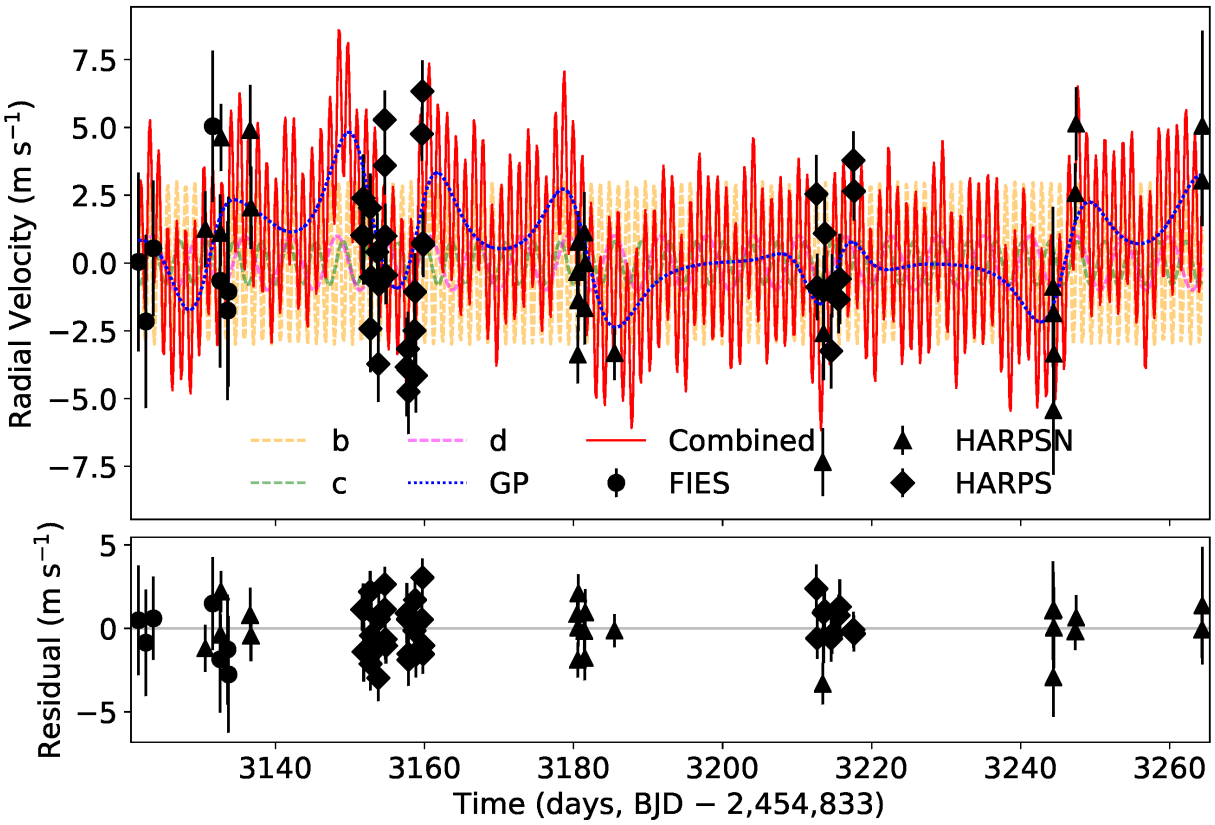

Fig. 7: The measured radial velocity variation of GJ 9827 from FIES (circles) and HARPS (diamonds) and HARPS-N (triangles). The red solid line is the best-fit model including the signal of the planets and the Gaussian Process model of the correlated stellar noise. The colored dashed line shows the signal of the planets. The blue dotted line shows the Gaussian Process model of correlated stellar noise.

cesses. For GJ 9827 b, c, and d we calculated an incident flux relative to the Earth's of 256, 59 and 29, respectively. Interestingly although there is only a factor two between the flux of the second and third planet, the later seems to have a much lower density. This third planet lies well above the atmospheric loss frontier described in Figure 10 of Van Eylen et al. (2017), while the other two are below. Moreover, the ratio between the incident fluxes and the masses of the planets are 70, 41 and 12, respectively. It is clear that the conditions of planet d are remarkably different from the other two.

However, the low density of planet d seems to defy the photoevaporation models. With a mass of $3M_{\oplus}$, previous models (Lammer et al. 2003; Owen and Wu 2016; Wang and Ji 2017) would predict that planet d lost its H/He envelope within the first 100 Myr of star's lifetime. We encourage more additional RV follow-up and transmission spectroscopy to pin down the properties of planet d. The results may clarify our understanding of the photoevaporation process or unveil additional processes such as extreme out-gassing or late migration of planet.

Given the brightness of the host star and small periods of the planets, the three planets transiting GJ 9827 are excellent targets for atmospheric characterization using both space and ground-based facilities. Niraula et al. (2017) calculated the expected S/N of a planetary atmosphere using masses estimated by the mass-radius relationship by Weiss and Marcy (2014) and using a method similar to Gillon et al. (2016). Since we found that the masses are smaller than estimated from the mass-radius relation, these planets become even more attractive candidates for atmospheric studies than originally predicted. This is because the low surface gravity leads to a larger scale height, and thereby a larger atmospheric signal. GJ 9827 d ranks as the fourth best candidate overall (behind GJ 1214 b, 55 Cnc e, and TRAPPIST-1 b), and GJ 9827 b and c rank sixth and seventh, respectively, among the 601 transiting planets with radii $<3R_{\oplus}$, as shown in Figure 10. This makes the GJ 9827 system a unique target for atmospheric studies.

7. Conclusions

We have presented the characterization and mass determination of the three planets orbiting GJ 9827 (Niraula et al. 2017; Rodriguez et al. 2018). GJ 9827 is a moderately active K6 V star (S-index$\approx$0.7) with a rotational period of $P_{\rm rot} \approx 30$ days transited by three small planets with masses of 3.74, 1.47, and 2.38 $M_{\oplus}$, determined with a precision of 7.5σ, 2.4σ, and 3.4σ, respectively. The system is an ideal laboratory to study planetary formation models and atmospheric photoevaporation. The densities

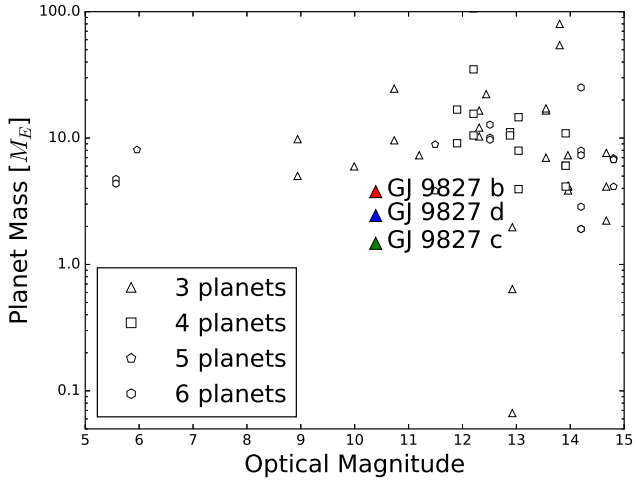

Fig. 8: Brightness-mass plot of planets with measured mass in multiple systems known to host at least three planets. With three transiting planets and V=10.35 mag, GJ 9827 is the brightest multi-planet transiting system for which the masses of all planets have been measured.

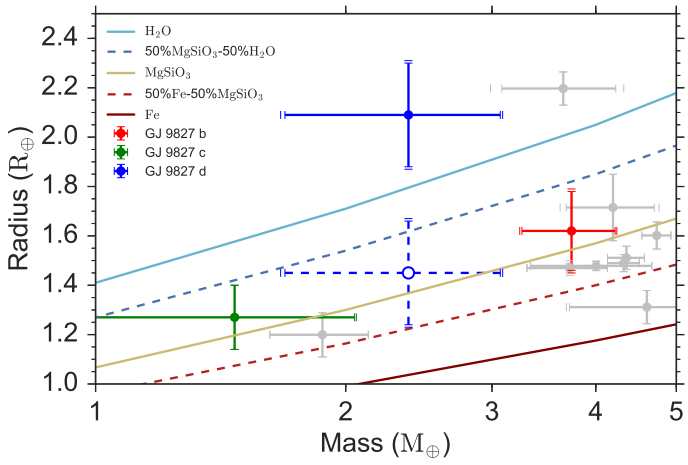

Fig. 9: A mass-radius diagram for all rocky planets with masses between 1-5 $M_\oplus$ and radii between 1-2.5 $R_\oplus$, as registered in the TEPCat database. The solid circles indicate measurements of the mass and radius of the planets of GJ 9827. The empty circle shows the inferred mass y radius of the nucleus of the third planet under the assumptions made on section 6.1.

of the three planets and the 1:3:5 orbital period ratio suggest an *in-situ* formation scenario.

Our findings indicate that the third planet – namely GJ 9827 d – might have an extended atmosphere. The brightness of the host star (V=10.35 mag, J=7.984 mag) makes the transiting system around GJ 9827 an ideal target to study the atmosphere of the three planets, using, for instance, JWST and ELT. By measuring the chemical abundances of the planetary atmospheres, it will be possible to further constrain the formation scenario of this system. Combining all this information, we will eventually unveil whether the planets formed roughly where they are found today, or whether they formed at much larger distance and then migrated inwards.

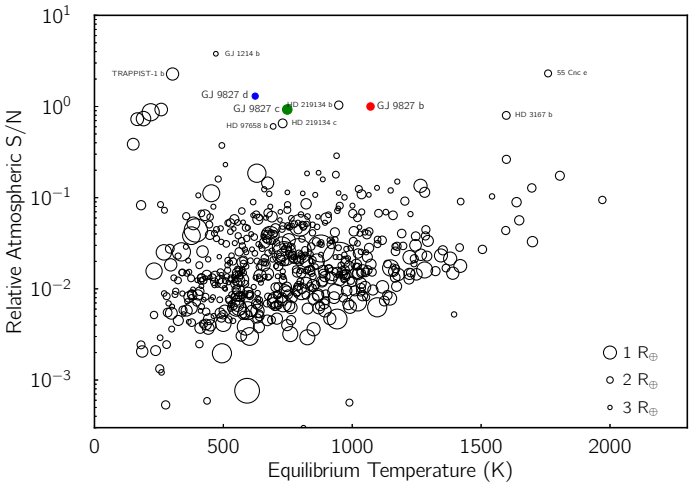

Fig. 10: The normalized atmospheric S/N for transiting planets with radii less than 3$R_\oplus$ as registered in the NASA Exoplanet Archive.

Acknowledgements. This work is partly financed by the Spanish Ministry of Economics and Competitiveness through projects ESP2014-57495-C2-1-R, ESP2016-80435-C2-2-R, and ESP2015-65712-C5-4-R of the Spanish Secretary of State for R&D&i (MINECO). This project has received funding from the European Union's Horizon 2020 research and innovation programme under grant agreement No 730890. This material reflects only the authors views and the Commission is not liable for any use that may be made of the information contained therein. DG gratefully acknowledges the financial support of the *Programma Giovani Ricercatori – Rita Levi Montalcini – Rientro dei Cervelli (2012)* awarded by the Italian Ministry of Education, Universities and Research (MIUR). SzCs, APH, MP, and HR acknowledge the support of the DFG priority program SPP 1992 "Exploring the Diversity of Extrasolar Planets" (HA 3279/12-1, PA 525/18-1, RA 714/14-1). I.R. acknowledges support from the Spanish Ministry of Economy and Competitiveness (MINECO) and the Fondo Europeo de Desarrollo Regional (FEDER) through grant ESP2016-80435-C2-1-R, as well as the support of the Generalitat de Catalunya/CERCA programme. This research has made use of the SIMBAD database, operated at CDS, Strasbourg, France.

References

Baranne, A., Queloz, D., Mayor, M., Adrianzyk, G., Knispel, G., Kohler, D., Lacroix, D., Meunier, J.-P., Rimbaud, G., and Vin, A. (1996). ELODIE: A spectrograph for accurate radial velocity measurements. *A&AS*, 119:373–390.

Barragán, O., Gandolfi, D., and Antoniciello, G. (2017). pyaneti: Multi-planet radial velocity and transit fitting. Astrophysics Source Code Library.

Barragán, O., Gandolfi, D., Smith, A. M. S., Deeg, H. J., Fridlund, M. C. V., Persson, C. M., Donati, P., Endl, M., Csizmadia, S., Grziwa, S., Nespral, D., Hatzes, A. P., Cochran, W. D., Fossati, L., Brems, S. S., Cabrera, J., Cusano, F., Eigmüller, P., Eiroa, C., Erikson, A., Guenther, E., Korth, J., Lorenzo-Oliveira, D., Mancini, L., Pätzold, M., Prieto-Arranz, J., Rauer, H., Rebollido, I., Saario, J., and Zakhozhay, O. V. (2018). K2-139 b: a low-mass warm Jupiter on a 29-d orbit transiting an active K0 V star. *MNRAS*, 475:1765–1776.

Barragán, O., Grziwa, S., Gandolfi, D., Fridlund, M., Endl, M., Deeg, H. J., Cagigal, M. P., Lanza, A. F., Prada Moroni, P. G., Smith, A. M. S., Korth, J., Bedell, M., Cabrera, J., Cochran, W. D., Cusano, F., Csizmadia, S., Eigmüller, P., Erikson, A., Guenther, E. W., Hatzes, A. P., Nespral, D., Pätzold, M., Prieto-Arranz, J., and Rauer, H. (2016). EPIC 211391664b: A 32 $M_\oplus$ Neptune-size Planet in a 10 Day Orbit Transiting an F8 Star. *AJ*, 152:193.

Baruteau, C., Crida, A., Paardekooper, S.-J., Masset, F., Guilet, J., Bitsch, B., Nelson, R., Kley, W., and Papaloizou, J. (2014). Planet-Disk Interactions and Early Evolution of Planetary Systems. *Protostars and Planets VI*, pages 667–689.

Broeg, C., Fortier, A., Ehrenreich, D., Alibert, Y., Baumjohann, W., Benz, W., Deleuil, M., Gillon, M., Ivanov, A., Liseau, R., Meyer, M., Oloffson, G., Pagano, I., Piotto, G., Pollacco, D., Queloz, D., Ragazzoni, R., Renotte, E., Steller, M., and Thomas, N. (2013). CHEOPS: A transit photometry mission

Table 5: Summary of the system parameters of GJ 9827 determined in section 5 with both methods: Pyaneti and Gaussian Process. We adopt the former values for the Discussion section.

Parameter	GJ 9827 b	GJ 9827 c	GJ 9827 d	Sinusoidal signal
Model Parameters: Pyaneti				
Orbital period $P_{\rm orb}$ (days)	$1.208966^{+0.000012}_{-0.000012}$	$3.648227^{+0.000117}_{-0.000119}$	$6.201419^{+0.000128}_{-0.000128}$	$14.460^{+0.105}_{-0.106}$
Transit epoch T_0 ($\rm BJD_{TDB}-2\,450\,000$)	$7738.82646^{+0.00044}_{-0.00042}$	$7738.54961^{+0.00146}_{-0.00145}$	$7740.96198^{+0.00084}_{-0.00086}$	$7739.87^{+1.96}_{-1.92}$
Scaled planet radius $R_{\rm p}/R_\star$	$0.02323^{+0.00058}_{-0.00037}$	$0.01820^{+0.00054}_{-0.00041}$	$0.02993^{+0.00101}_{-0.00078}$	...
Impact parameter, b	$0.21^{+0.23}_{-0.14}$	$0.25^{+0.21}_{-0.16}$	$0.864^{+0.022}_{-0.013}$	...
$\sqrt{e}\sin\omega_\star^{(a)}$	0	0	0	
$\sqrt{e}\cos\omega_\star^{(a)}$	0	0	0	
Doppler semi-amplitude variation K ($\rm m\,s^{-1}$)	3.00 ± 0.35	0.82 ± 0.32	1.11 ± 0.32	3.15 ± 0.44
Stellar density parametrization $\rho_\star^{1/3}$ ($\rm g^{1/3}\,cm^{-1}$)	$1.697^{+0.044}_{-0.128}$			
Systemic velocity $\gamma_{\rm FIES}$ ($\rm km\,s^{-1}$)	$31.77374^{+0.00136}_{-0.00139}$			
Systemic velocity $\gamma_{\rm HARPS}$ ($\rm km\,s^{-1}$)	$31.94794^{+0.00036}_{-0.00037}$			
Systemic velocity $\gamma_{\rm HARPS-N}$ ($\rm km\,s^{-1}$)	$31.94888^{+0.00035}_{-0.00034}$			
jitter $\sigma_{\rm FIES}$ ($\rm m\,s^{-1}$)	$1.25^{+1.55}_{-0.89}$			
jitter $\sigma_{\rm HARPS}$ ($\rm m\,s^{-1}$)	$0.96^{+0.37}_{-0.39}$			
jitter $\sigma_{\rm HARPS-N}$ ($\rm m\,s^{-1}$)	$0.61^{+0.48}_{-0.40}$			
Parameterized limb-darkening coefficient $q_1^{(b)}$	$0.531^{+0.091}_{-0.089}$			
Parameterized limb-darkening coefficient $q_2^{(b)}$	$0.398^{+0.087}_{-0.086}$			
Derived Parameters: Pyaneti				
Planet mass $M_{\rm p}$ ($M_\oplus$)	$3.74^{+0.50}_{-0.48}$	$1.47^{+0.59}_{-0.58}$	$2.38^{+0.71}_{-0.69}$	...
Planet radius $R_{\rm p}$ ($R_\oplus$)	$1.62^{+0.17}_{-0.16}$	$1.27^{+0.13}_{-0.13}$	$2.09^{+0.22}_{-0.21}$	...
Planet density $\rho_{\rm p}$ ($\rm g\,cm^{-3}$)	$4.81^{+1.97}_{-1.33}$	$3.87^{+2.38}_{-1.71}$	$1.42^{+0.75}_{-0.52}$	...
Surface gravity $g_{\rm p}$ ($\rm cm\,s^{-2}$)	1395^{+391}_{-298}	887^{+446}_{-369}	534^{+219}_{-175}	
Surface gravity$^{(c)}$ $g_{\rm p}$ ($\rm cm\,s^{-2}$)	1712^{+264}_{-354}	1062^{+478}_{-461}	641^{+225}_{-223}	
Scaled semi-major axis $a/R_\star$	$7.23^{+0.19}_{-0.55}$	$15.10^{+0.39}_{-1.14}$	$21.50^{+0.56}_{-1.63}$	...
Semi-major axis a (AU)	$0.0210^{+0.0024}_{-0.0026}$	$0.0439^{+0.0050}_{-0.0055}$	$0.0625^{+0.0071}_{-0.0078}$	...
Orbit inclination $i_{\rm p}$ (°)	$88.33^{+1.15}_{-2.10}$	$89.07^{+0.59}_{-0.92}$	$87.703^{+0.081}_{-0.253}$	...
Transit duration τ_{14} (hours)	$1.281^{+0.020}_{-0.019}$	$1.825^{+0.042}_{-0.042}$	$1.248^{+0.038}_{-0.033}$	
Equilibrium temperature$^{(d)}$ $T_{\rm eq}$ (K)	1114^{+46}_{-26}	771^{+32}_{-18}	646^{+26}_{-15}	
Insolation F ($F_\oplus$)	256^{+45}_{-23}	59^{+10}_{-5}	29^{+5}_{-3}	
Stellar density (from light curve)	$4.89^{+0.39}_{-1.03}$			
Linear limb-darkening coefficient u_1	$0.577^{+0.125}_{-0.125}$			
Quadratic limb-darkening coefficient u_2	$0.147^{+0.131}_{-0.126}$			
Model Parameters: Gaussian Process				
Doppler semi-amplitude variation K ($\rm m\,s^{-1}$)	3.41 ± 0.53	< 1.10	1.06 ± 0.52	$2.30^{0.97}_{0.66}$

Note – [(a)] Fixed to zero. [(b)] q_1 and q_2 as defined by Kipping (2013). [(c)] Calculated from the scaled parameters as described by Winn (2010). [(d)] Assuming albedo = 0.

for ESA's small mission programme. In *European Physical Journal Web of Conferences*, volume 47 of *European Physical Journal Web of Conferences*, page 03005.

Bruntt, H., Bedding, T. R., Quirion, P.-O., Lo Curto, G., Carrier, F., Smalley, B., Dall, T. H., Arentoft, T., Bazot, M., and Butler, R. P. (2010). Accurate fundamental parameters for 23 bright solar-type stars. *MNRAS*, 405:1907–1923.

Chiang, E. and Laughlin, G. (2013). The minimum-mass extrasolar nebula: in situ formation of close-in super-Earths. *MNRAS*, 431:3444–3455.

Cosentino, R., Lovis, C., Pepe, F., Collier Cameron, A., Latham, D. W., Molinari, E., Udry, S., Bezawada, N., Black, M., Born, A., Buchschacher, N., Charbonneau, D., Figueira, P., Fleury, M., Galli, A., Gallie, A., Gao, X., Ghedina, A., Gonzalez, C., Gonzalez, M., Guerra, J., Henry, D., Horne, K., Hughes, I., Kelly, D., Lodi, M., Lunney, D., Maire, C., Mayor, M., Micela, G., Ordway, M. P., Peacock, J., Phillips, D., Piotto, G., Pollacco, D., Queloz, D., Rice, K., Riverol, C., Riverol, L., San Juan, J., Sasselov, D., Segransan, D., Sozzetti, A., Sosnowska, D., Stobie, B., Szentgyorgyi, A., Vick, A., and Weber, L. (2012). Harps-N: the new planet hunter at TNG. In *Ground-based and Airborne Instrumentation for Astronomy IV*, volume 8446 of *Proc. SPIE*, page 84461V.

Dai, F., Winn, J. N., Gandolfi, D., Wang, S. X., Teske, J. K., Burt, J., Albrecht, S., Barragán, O., Cochran, W. D., Endl, M., Fridlund, M., Hatzes, A. P., Hirano, T., Hirsch, L. A., Johnson, M. C., Justesen, A. B., Livingston, J., Persson, C. M., Prieto-Arranz, J., Vanderburg, A., Alonso, R., Antoniciello, G., Arriagada, P., Butler, R. P., Cabrera, J., Crane, J. D., Cusano, F., Csizmadia, S., Deeg, H., Dieterich, S. B., Eigmüller, P., Erikson, A., Everett, M. E., Fukui, A., Grziwa, S., Guenther, E. W., Henry, G. W., Howell, S. B., Johnson, J. A., Korth, J., Kuzuhara, M., Narita, N., Nespral, D., Nowak, G., Palle, E., Pätzold, M., Rauer, H., Montañés Rodríguez, P., Shectman, S. A., Smith, A. M. S., Thompson, I. B., Van Eylen, V., Williamson, M. W., and Wittenmyer, R. A. (2017). The Discovery and Mass Measurement of a New Ultra-short-period Planet: K2-131b. *AJ*, 154:226.

Dumusque, X., Boisse, I., and Santos, N. C. (2014). SOAP 2.0: A Tool to Estimate the Photometric and Radial Velocity Variations Induced by Stellar Spots and Plages. *ApJ*, 796:132.

Foreman-Mackey, D., Hogg, D. W., Lang, D., and Goodman, J. (2013). emcee: The MCMC Hammer. *PASP*, 125:306.

Frandsen, S. and Lindberg, B. (1999). FIES: A high resolution FIber fed Echelle Spectrograph for the NOT (poster). In Karttunen, H. and Piirola, V., editors, *Astrophysics with the NOT*, page 71.

Fridlund, M., Gaidos, E., Barragán, O., Persson, C. M., Gandolfi, D., Cabrera, J., Hirano, T., Kuzuhara, M., Csizmadia, S., Nowak, G., Endl, M., Grziwa, S., Korth, J., Pfaff, J., Bitsch, B., Johansen, A., Mustill, A. J., Davies, M. B., Deeg, H. J., Palle, E., Cochran, W. D., Eigmüller, P., Erikson, A., Guenther, E., Hatzes, A. P., Kiilerich, A., Kudo, T., MacQueen, P., Narita, N., Nespral, D., Pätzold, M., Prieto-Arranz, J., Rauer, H., and Van Eylen, V. (2017). K2-111 b - a short period super-Earth transiting a metal poor, evolved old star. *A&A*, 604:A16.

Fuhrmann, K., Axer, M., and Gehren, T. (1993). Balmer lines in cool dwarf stars. 1. Basic influence of atmospheric models. *A&A*, 271:451.

Fuhrmann, K., Axer, M., and Gehren, T. (1994). Balmer lines in cool dwarf stars II. Effective temperatures and calibration of colour indices. *A&A*, 285:585–594.

Fulton, B. J., Petigura, E. A., Howard, A. W., Isaacson, H., Marcy, G. W., Cargile, P. A., Hebb, L., Weiss, L. M., Johnson, J. A., Morton, T. D., Sinukoff, E., Crossfield, I. J. M., and Hirsch, L. A. (2017). The California-Kepler Survey. III. A Gap in the Radius Distribution of Small Planets. *AJ*, 154:109.

Gandolfi, D., Alcalá, J. M., Leccia, S., Frasca, A., Spezzi, L., Covino, E., Testi, L., Marilli, E., and Kainulainen, J. (2008). The Star Formation in the L1615/L1616 Cometary Cloud. *ApJ*, 687:1303–1322.

Gandolfi, D., Barragán, O., Hatzes, A. P., Fridlund, M., Fossati, L., Donati, P., Johnson, M. C., Nowak, G., Prieto-Arranz, J., Albrecht, S., Dai, F., Deeg, H., Endl, M., Grziwa, S., Hjorth, M., Korth, J., Nespral, D., Saario, J., Smith, A. M. S., Antoniciello, G., Alarcon, J., Bedell, M., Blay, P., Brems, S. S., Cabrera, J., Csizmadia, S., Cusano, F., Cochran, W. D., Eigmüller, P., Erikson, A., González Hernández, J. I., Guenther, E. W., Hirano, T., Suárez Mascareño, A., Narita, N., Palle, E., Parviainen, H., Pätzold, M., Persson, C. M., Rauer, H., Saviane, I., Schmidtobreick, L., Van Eylen, V., Winn, J. N., and Zakhozhay, O. V. (2017). The Transiting Multi-planet System HD 3167: A 5.7 $M_\oplus$ Super-Earth and an 8.3 $M_\oplus$ Mini-Neptune. *AJ*, 154:123.

Gillon, M., Jehin, E., Lederer, S. M., Delrez, L., de Wit, J., Burdanov, A., Van Grootel, V., Burgasser, A. J., Triaud, A. H. M. J., Opitom, C., Demory, B.-O., Sahu, D. K., Bardalez Gagliuffi, D., Magain, P., and Queloz, D. (2016). Temperate Earth-sized planets transiting a nearby ultracool dwarf star. *Nature*, 533:221–224.

Gontcharov, G. A. and Mosenkov, A. V. (2018). Verifying reddening and extinction for Gaia DR1 TGAS giants. *MNRAS*, 475:1121–1130.

Gray, D. F. (2008). *The Observation and Analysis of Stellar Photospheres*. Cambridge University Press.

Grunblatt, S. K., Howard, A. W., and Haywood, R. D. (2015). Determining the Mass of Kepler-78b with Nonparametric Gaussian Process Estimation. *ApJ*, 808:127.

Guenther, E. W., Barragán, O., Dai, F., Gandolfi, D., Hirano, T., Fridlund, M., Fossati, L., Chau, A., Helled, R., Korth, J., Prieto-Arranz, J., Nespral, D., Antoniciello, G., Deeg, H., Hjorth, M., Grziwa, S., Albrecht, S., Hatzes, A. P., Rauer, H., Csizmadia, S., Smith, A. M. S., Cabrera, J., Narita, N., Arriagada, P., Burt, J., Butler, R. P., Cochran, W. D., Crane, J. D., Eigmüller, P., Erikson, A., Johnson, J. A., Kiilerich, A., Kubyshkina, D., Palle, E., Persson, C. M., Pätzold, M., Sabotta, S., Sato, B., Shectman, S. A., Teske, J. K., Thompson, I. B., Van Eylen, V., Nowak, G., Vanderburg, A., Winn, J. N., and Wittenmyer, R. A. (2017). K2-106, a system containing a metal-rich planet and a planet of lower density. *A&A*, 608:A93.

Hansen, B. M. S. and Murray, N. (2013). Testing in Situ Assembly with the Kepler Planet Candidate Sample. *ApJ*, 775:53.

Hatzes, A. P., Dvorak, R., Wuchterl, G., Guterman, P., Hartmann, M., Fridlund, M., Gandolfi, D., Guenther, E., and Pätzold, M. (2010). An investigation into the radial velocity variations of CoRoT-7. *A&A*, 520:A93.

Haywood, R. D. (2015). *Hide and Seek: Radial-Velocity Searches for Planets around Active Stars*. PhD thesis, University of St Andrews.

Haywood, R. D., Collier Cameron, A., Queloz, D., Barros, S. C. C., Deleuil, M., Fares, R., Gillon, M., Lanza, A. F., Lovis, C., Moutou, C., Pepe, F., Pollacco, D., Santerne, A., Ségransan, D., and Unruh, Y. C. (2014). Planets and stellar activity: hide and seek in the CoRoT-7 system. *MNRAS*, 443:2517–2531.

Hirano, T., Dai, F., Gandolfi, D., Fukui, A., Livingston, J. H., Miyakawa, K., Endl, M., Cochran, W. D., Alonso-Floriano, F. J., Kuzuhara, M., Montes, D., Ryu, T., Albrecht, S., Barragan, O., Cabrera, J., Csizmadia, S., Deeg, H., Eigmüller, P., Erikson, A., Fridlund, M., Grziwa, S., Guenther, E. W., Hatzes, A. P., Korth, J., Kudo, T., Kusakabe, N., Narita, N., Nespral, D., Nowak, G., Pätzold, M., Palle, E., Persson, C. M., Prieto-Arranz, J., Rauer, H., Ribas, I., Sato, B., Smith, A. M. S., Tamura, M., Tanaka, Y., Van Eylen, V., and Winn, J. N. (2017). Exoplanets around Low-mass Stars Unveiled by K2. *ArXiv e-prints*.

Houdebine, E. R., Mullan, D. J., Paletou, F., and Gebran, M. (2016). Rotation-Activity Correlations in K and M Dwarfs. I. Stellar Parameters and Compilations of v sin I and P/sin I for a Large Sample of Late-K and M Dwarfs. *ApJ*, 822:97.

Howell, S. B., Everett, M. E., Sherry, W., Horch, E., and Ciardi, D. R. (2011). Speckle Camera Observations for the NASA Kepler Mission Follow-up Program. *AJ*, 142:19.

Izidoro, A., Ogihara, M., Raymond, S. N., Morbidelli, A., Pierens, A., Bitsch, B., Cossou, C., and Hersant, F. (2017). Breaking the chains: hot super-Earth systems from migration and disruption of compact resonant chains. *MNRAS*, 470:1750–1770.

Kipping, D. M. (2010). Binning is sinning: morphological light-curve distortions due to finite integration time. *MNRAS*, 408:1758–1769.

Kipping, D. M. (2013). Efficient, uninformative sampling of limb darkening coefficients for two-parameter laws. *MNRAS*, 435:2152–2160.

Kuerster, M., Schmitt, J. H. M. M., Cutispoto, G., and Dennerl, K. (1997). ROSAT and AB Doradus: the first five years. *A&A*, 320:831–839.

Kurucz, R. L. (2013). ATLAS12: Opacity sampling model atmosphere program. Astrophysics Source Code Library.

Lammer, H., Selsis, F., Ribas, I., Guinan, E. F., Bauer, S. J., and Weiss, W. W. (2003). Atmospheric Loss of Exoplanets Resulting from Stellar X-Ray and Extreme-Ultraviolet Heating. *ApJ*, 598:L121–L124.

Lopez, E. D. (2017). Kepler's Rocky Exoplanets: Born Rocky or Stripped Sub-Neptunes? *LPI Contributions*, 2042:4129.

López-Morales, M., Haywood, R. D., Coughlin, J. L., Zeng, L., Buchhave, L. A., Giles, H. A. C., Affer, L., Bonomo, A. S., Charbonneau, D., Collier Cameron, A., Consentino, R., Dressing, C. D., Dumusque, X., Figueira, P., Fiorenzano, A. F. M., Harutyunyan, A., Johnson, J. A., Latham, D. W., Lopez, E. D., Lovis, C., Malavolta, L., Mayor, M., Micela, G., Molinari, E., Mortier, A., Motalebi, F., Nascimbeni, V., Pepe, F., Phillips, D. F., Piotto, G., Pollacco, D., Queloz, D., Rice, K., Sasselov, D., Segransan, D., Sozzetti, A., Udry, S., Vanderburg, A., and Watson, C. (2016). Kepler-21b: A Rocky Planet Around a V = 8.25 Magnitude Star. *AJ*, 152:204.

Mandel, K. and Agol, E. (2002). Analytic Light Curves for Planetary Transit Searches. *ApJ*, 580:L171–L175.

Mann, A. W., Feiden, G. A., Gaidos, E., Boyajian, T., and von Braun, K. (2015). How to Constrain Your M Dwarf: Measuring Effective Temperature, Bolometric Luminosity, Mass, and Radius. *ApJ*, 804:64.

Marzari, F. and Weidenschilling, S. (2002). Mean Motion Resonances, Gas Drag, and Supersonic Planetesimals in the Solar Nebula. *Celestial Mechanics and Dynamical Astronomy*, 82:225–242.

Masset, F. S., Morbidelli, A., Crida, A., and Ferreira, J. (2006). Disk Surface Density Transitions as Protoplanet Traps. *ApJ*, 642:478–487.

Mayor, M., Pepe, F., Queloz, D., Bouchy, F., Rupprecht, G., Lo Curto, G., Avila, G., Benz, W., Bertaux, J.-L., Bonfils, X., Dall, T., Dekker, H., Delabre, B., Eckert, W., Fleury, M., Gilliotte, A., Gojak, D., Guzman, J. C., Kohler, D., Lizon, J.-L., Longinotti, A., Lovis, C., Megevand, D., Pasquini, L., Reyes, J., Sivan, J.-P., Sosnowska, D., Soto, R., Udry, S., van Kesteren, A., Weber, L., and Weilenmann, U. (2003). Setting New Standards with HARPS. *The Messenger*, 114:20–24.

McDonald, I., Zijlstra, A. A., and Watson, R. A. (2017). Fundamental parameters and infrared excesses of Tycho-Gaia stars. *MNRAS*, 471:770–791.

Mumford, G. S. (1956). Photoelectric observations of red dwarf stars. *AJ*, 61:213–218.

Niraula, P., Redfield, S., Dai, F., Barragán, O., Gandolfi, D., Cauley, P. W., Hirano, T., Korth, J., Smith, A. M. S., Prieto-Arranz, J., Grziwa, S., Fridlund, M., Persson, C. M., Justesen, A. B., Winn, J. N., Albrecht, S., Cochran, W. D., Csizmadia, S., Duvvuri, G. M., Endl, M., Hatzes, A. P., Livingston, J. H., Narita, N., Nespral, D., Nowak, G., Pätzold, M., Palle, E., and Van Eylen, V. (2017). Three Super-Earths Transiting the Nearby Star GJ 9827. *AJ*, 154:266.

Nowak, G., Palle, E., Gandolfi, D., Dai, F., Lanza, A. F., Hirano, T., Barragán, O., Fukui, A., Bruntt, H., Endl, M., Cochran, W. D., Prada Moroni, P. G., Prieto-Arranz, J., Kiilerich, A., Nespral, D., Hatzes, A. P., Albrecht, S., Deeg, H., Winn, J. N., Yu, L., Kuzuhara, M., Grziwa, S., Smith, A. M. S., Guenther, E. W., Van Eylen, V., Csizmadia, S., Fridlund, M., Cabrera, J., Eigmüller, P., Erikson, A., Korth, J., Narita, N., Pätzold, M., Rauer, H., and Ribas, I. (2017). EPIC 219388192b — An Inhabitant of the Brown Dwarf Desert in the Ruprecht 147 Open Cluster. *AJ*, 153:131.

Owen, J. E. and Wu, Y. (2016). Atmospheres of Low-mass Planets: The "Boil-off". *ApJ*, 817:107.

Pepe, F., Cristiani, S., Rebolo, R., Santos, N. C., Dekker, H., Mégevand, D., Zerbi, F. M., Cabral, A., Molaro, P., Di Marcantonio, P., Abreu, M., Affolter, M., Aliverti, M., Allende Prieto, C., Amate, M., Avila, G., Baldini, V., Bristow, P., Broeg, C., Cirami, R., Coelho, J., Conconi, P., Coretti, I., Cupani, G., D'Odorico, V., De Caprio, V., Delabre, B., Dorn, R., Figueira, P., Fragoso, A., Galeotta, S., Genolet, L., Gomes, R., González Hernández, J. I., Hughes, I., Iwert, O., Kerber, F., Landoni, M., Lizon, J.-L., Lovis, C., Maire, C., Mannetta, M., Martins, C., Monteiro, M. A., Oliveira, A., Poretti, E., Rasilla, J. L., Riva, M., Santana Tschudi, S., Santos, P., Sosnowska, D., Sousa, S., Spanò, P., Tenegi, F., Toso, G., Vanzella, E., Viel, M., and Zapatero Osorio, M. R. (2013). ESPRESSO — An Echelle SPectrograph for Rocky Exoplanets Search and Stable Spectroscopic Observations. *The Messenger*, 153:6–16.

Pepe, F., Mayor, M., Galland, F., Naef, D., Queloz, D., Santos, N. C., Udry, S., and Burnet, M. (2002). The CORALIE survey for southern extra-solar planets VII. Two short-period Saturnian companions to ¡ASTROBJ¿HD 108147¡/ASTROBJ¿ and ¡ASTROBJ¿HD 168746¡/ASTROBJ¿. *A&A*, 388:632–638.

Rauer, H. (2017). The PLATO Mission. In *EGU General Assembly Conference Abstracts*, volume 19 of *EGU General Assembly Conference Abstracts*, page 4829.

Raymond, S. N., Barnes, R., and Mandell, A. M. (2008). Observable consequences of planet formation models in systems with close-in terrestrial plan-

ets. *MNRAS*, 384:663–674.
Rodriguez, J. E., Vanderburg, A., Eastman, J. D., Mann, A. W., Crossfield, I. J. M., Ciardi, D. R., Latham, D. W., and Quinn, S. N. (2018). A System of Three Super Earths Transiting the Late K-Dwarf GJ 9827 at 30 pc. *AJ*, 155:72.
Scott, N. J., Howell, S. B., and Horch, E. P. (2016). Differential speckle and wide-field imaging for the Gemini-North and WIYN telescopes. In *Optical and Infrared Interferometry and Imaging V*, volume 9907 of *Proc. SPIE*, page 99072R.
Skrutskie, M. F., Cutri, R. M., Stiening, R., Weinberg, M. D., Schneider, S., Carpenter, J. M., Beichman, C., Capps, R., Chester, T., Elias, J., Huchra, J., Liebert, J., Lonsdale, C., Monet, D. G., Price, S., Seitzer, P., Jarrett, T., Kirkpatrick, J. D., Gizis, J. E., Howard, E., Evans, T., Fowler, J., Fullmer, L., Hurt, R., Light, R., Kopan, E. L., Marsh, K. A., McCallon, H. L., Tam, R., Van Dyk, S., and Wheelock, S. (2006). The Two Micron All Sky Survey (2MASS). *AJ*, 131:1163–1183.
Sun, Z., Ji, J., Wang, S., and Jin, S. (2017). Terrestrial planet formation under migration: systems near the 4:2:1 mean motion resonance. *MNRAS*, 467:619–632.
Telting, J. H., Avila, G., Buchhave, L., Frandsen, S., Gandolfi, D., Lindberg, B., Stempels, H. C., Prins, S., and NOT staff (2014). FIES: The high-resolution Fiber-fed Echelle Spectrograph at the Nordic Optical Telescope. *Astronomische Nachrichten*, 335:41.
Thiabaud, A., Marboeuf, U., Alibert, Y., Leya, I., and Mezger, K. (2015). Gas composition of the main volatile elements in protoplanetary discs and its implication for planet formation. *A&A*, 574:A138.
Valenti, J. A. and Fischer, D. A. (2005). Spectroscopic Properties of Cool Stars (SPOCS). I. 1040 F, G, and K Dwarfs from Keck, Lick, and AAT Planet Search Programs. *ApJS*, 159:141–166.
Valenti, J. A. and Piskunov, N. (1996). Spectroscopy made easy: A new tool for fitting observations with synthetic spectra. *A&AS*, 118:595–603.
Van Eylen, V., Agentoft, C., Lundkvist, M. S., Kjeldsen, H., Owen, J. E., Fulton, B. J., Petigura, E., and Snellen, I. (2017). An asteroseismic view of the radius valley: stripped cores, not born rocky. *ArXiv e-prints*.
Van Eylen, V. and Albrecht, S. (2015). Eccentricity from Transit Photometry: Small Planets in Kepler Multi-planet Systems Have Low Eccentricities. *ApJ*, 808:126.
van Leeuwen, F. (2007). Validation of the new Hipparcos reduction. *A&A*, 474:653–664.
Wang, S. and Ji, J. (2017). Near Mean-motion Resonances in the System Observed by Kepler: Affected by Mass Accretion and Type I Migration. *AJ*, 154:236.
Weiss, L. M. and Marcy, G. W. (2014). The Mass-Radius Relation for 65 Exoplanets Smaller than 4 Earth Radii. *ApJ*, 783:L6.
Winn, J. N. (2010). *Exoplanet Transits and Occultations*, pages 55–77. University of Arizona Press.
Winn, J. N. and Fabrycky, D. C. (2015). The Occurrence and Architecture of Exoplanetary Systems. *ARA&A*, 53:409–447.
Wolfgang, A. and Lopez, E. (2015). How Rocky Are They? The Composition Distribution of Kepler's Sub-Neptune Planet Candidates within 0.15 AU. *ApJ*, 806:183.
Wurm, G., Trieloff, M., and Rauer, H. (2013). Photophoretic Separation of Metals and Silicates: The Formation of Mercury-like Planets and Metal Depletion in Chondrites. *ApJ*, 769:78.
Yee, S. W., Petigura, E. A., and von Braun, K. (2017). Precision Stellar Characterization of FGKM Stars using an Empirical Spectral Library. *ApJ*, 836:77.
Zechmeister, M. and Kürster, M. (2009). The generalised Lomb-Scargle periodogram. A new formalism for the floating-mean and Keplerian periodograms. *A&A*, 496:577–584.
Zeng, L., Sasselov, D. D., and Jacobsen, S. B. (2016). Mass-Radius Relation for Rocky Planets Based on PREM. *ApJ*, 819:127.

[1] Instituto de Astrofísica de Canarias (IAC), 38205 La Laguna, Tenerife, Spain e-mail: jparranz@iac.es
[2] Departamento de Astrofísica, Universidad de La Laguna (ULL), 38206, La Laguna, Tenerife, Spain
[3] Dipartimento di Fisica, Universitá di Torino, Via P. Giuria 1, I-10125, Torino, Italy
[4] Thüringer Landessternwarte Tautenburg, Sternwarte 5, 07778 Tautenburg, Germany
[5] Department of Astrophysical Sciences, Princeton University, 4 Ivy Lane, Princeton, NJ 08544, USA
[6] Department of Physics and Kavli Institute for Astrophysics and Space Research, Massachusetts Institute of Technology, Cambridge, MA 02139, USA
[7] Leiden Observatory, Leiden University, 2333CA Leiden, The Netherlands
[8] Department of Space, Earth and Environment, Chalmers University of Technology, Onsala Space Observatory, 439 92 Onsala, Sweden
[9] Department of Earth and Planetary Sciences, Tokyo Institute of Technology, 2-12-1 Ookayama, Meguro-ku, Tokyo 152-8551, Japan
[10] Department of Astronomy, The University of Tokyo, 7-3-1 Hongo, Bunkyo-ku, Tokyo 113-0033, Japan
[11] Astronomy Department and Van Vleck Observatory, Wesleyan University, Middletown, CT 06459, USA
[12] Stellar Astrophysics Centre, Department of Physics and Astronomy, Aarhus University, Ny Munkegade 120, DK-8000 Aarhus C, Denmark
[13] Institute of Planetary Research, German Aerospace Center, Rutherfordstrasse 2, 12489 Berlin, Germany
[14] Department of Astronomy and McDonald Observatory, University of Texas at Austin, 2515 Speedway, Stop C1400, Austin, TX 78712, USA
[15] National Optical Astronomy Observatory, 950 North Cherry Avenue, Tucson, AZ 85719, USA
[16] Okayama Astrophysical Observatory, National Astronomical Observatory of Japan, NINS, Asakuchi, Okayama 719-0232, Japan
[17] Rheinisches Institut für Umweltforschung an der Universität zu Köln, Aachener Strasse 209, 50931 Köln, Germany
[18] Universidade de São Paulo, Departamento de Astronomia do IAG/USP, Rua do Matão 1226, Cidade Universitária, 05508-900 São Paulo, SP, Brazil
[19] Astrobiology Center, NINS, 2-21-1 Osawa, Mitaka, Tokyo 181-8588, Japan
[20] National Astronomical Observatory of Japan, NINS, 2-21-1 Osawa, Mitaka, Tokyo 181-8588, Japan
[21] Center for Astronomy and Astrophysics, TU Berlin, Hardenbergstr. 36, 10623 Berlin, Germany
[22] Institut de Ciències de l´ Espai (IEEC-CSIC), C/Can Magrans, s/n, Campus UAB, 08193 Bellaterra, Spain
[23] Institut dEstudis Espacials de Catalunya (IEEC), E-08034 Barcelona, Spain

Table .1: FIES RV measurements of GJ 9827

BJD^1_{TDB} -2450000	RV ($km\,s^{-1}$)	$\pm\sigma$ ($km\,s^{-1}$)	BIS ($km\,s^{-1}$)	FWHM ($km\,s^{-1}$)	Ca II S index	$\pm\sigma$	T_{exp} (s)	S/N [2]
FIES								
7954.617085	31.7746	0.0033	-	-	-	-	2700	55.2
7955.612895	31.7724	0.0032	-	-	-	-	2700	56.0
7956.627456	31.7751	0.0025	-	-	-	-	2700	68.5
.....	.....	.....	-	-	-	-	....	....

Table .2: HARPS RV measurements of GJ 9827

BJD^1_{TDB} -2450000	RV ($km\,s^{-1}$)	$\pm\sigma$ ($km\,s^{-1}$)	BIS ($km\,s^{-1}$)	FWHM ($km\,s^{-1}$)	Ca II S index	$\pm\sigma$	T_{exp} (s)	S/N [2]
HARPS								
7984.653428	31.9468	0.0013	0.0603	6.1447	0.679	0.010	2000	79.9
7984.773491	31.9481	0.0016	0.0611	6.1409	0.662	0.016	1800	64.8
7984.843042	31.9467	0.0018	0.0586	6.1466	0.630	0.021	3600	60.3
.....	.....	.....	.....	.....	.....	.....	....	....

Table .3: HARPS-N RV measurements of GJ 9827

BJD^1_{TDB} -2450000	RV ($km\,s^{-1}$)	$\pm\sigma$ ($km\,s^{-1}$)	BIS ($km\,s^{-1}$)	FWHM ($km\,s^{-1}$)	Ca II S index	$\pm\sigma$	T_{exp} (s)	S/N [2]
HARPS-N								
7963.592670	31.9498	0.0014	0.0478	6.1011	0.700	0.010	1800	69.3
7965.613121	31.9496	0.0012	0.0456	6.1111	0.714	0.008	1800	77.9
7965.691320	31.9531	0.0012	0.0447	6.1120	0.746	0.008	1800	75.8
.....	.....	.....	.....	.....	.....	.....	....	....

Notes:
[1] Barycentric Julian dates are given in barycentric dynamical time.
[2] S/N per pixel at 550 nm.